

pubs.acs.org/JACS Communication

# Near-Infrared Dual Emission from the Au<sub>42</sub>(SR)<sub>32</sub> Nanocluster and **Tailoring of Intersystem Crossing**

Lianshun Luo, \* Zhongyu Liu, \* Xiangsha Du, and Rongchao Jin\*



Cite This: J. Am. Chem. Soc. 2022, 144, 19243-19247



**Read Online** 

ACCESS I

Metrics & More

Article Recommendations

Supporting Information

ABSTRACT: This work presents the synthesis and intriguing photoluminescence of the Au<sub>42</sub>(PET)<sub>32</sub> (PET = 2-phenylethanethiolate) nanocluster (NC). The Au<sub>42</sub>(PET)<sub>32</sub> NC exhibits dual emission at 875 and 1040 nm, which are revealed to be fluorescence and phosphorescence, respectively. The emission quantum yield (QY) of Au<sub>42</sub>(PET)<sub>32</sub> in dichloromethane is 11.9% at room temperature in air, which is quite rare for thiolate-protected Au NCs. When Au<sub>42</sub>(PET)<sub>32</sub> NCs are embedded in polystyrene films (solid state), the fluorescence was dramatically suppressed while the phosphorescence was significantly enhanced. This divergent behavior is explained by dipolar interaction-induced enhancement of intersystem crossing from singlet to triplet excited

Photoluminescence (PL) has long been of major interest in both fundamental research<sup>1-8</sup> and practical applications, 9-13 particularly, the dual emission phenomena for deciphering the underlying mechanisms and with great potentials in many fields, including ratiometric sensing, bioimaging, solar cells, and even supramolecular encryption systems. 14,15 Ultrasmall Au nanoparticles with atomic precision (1-3 nm in diameter), commonly called nanoclusters (NCs), show near-infrared (NIR) PL. 16-25 The determined atomic structures and electronic structure calculations<sup>26</sup> allow the elucidation of structure-property correlations, <sup>16-25</sup> and the intrinsic merits of Au NCs such as being biocompatible, stable, and nontoxic make this class of materials quite promising for solar energy conversion and biological applications.<sup>27–31</sup> So far, dual emission in Au NCs has only been observed in several bitetrahedral kernel structures, and the PL quantum yields (QYs) of those Au NCs in the NIR region were quite low  $(\sim 1\%)^{.18}$ 

Herein, we report the NIR dual emission of  $Au_{42}(PET)_{32}$ with a QY (11.9%) at room temperature under ambient conditions. The efficient dual emission of Au<sub>42</sub>(PET)<sub>32</sub> is rare for thiolate-protected Au NCs. The two emission peaks of Au<sub>42</sub>(PET)<sub>32</sub> at 875 and 1040 nm are fluorescence and phosphorescence, respectively. When Au<sub>42</sub>(PET)<sub>32</sub> NCs are embedded in polystyrene (PS) films, the QY of phosphorescence significantly increases from 8.6% to 20.3% while the fluorescence is suppressed from 3.2% to 1.1%. The mechanism involves dipolar interaction-induced intersystem crossing, which results in the observed divergent behavior of fluorescence and phosphorescence.

Different from the reported synthesis method,<sup>32</sup> here we used a NHC-Au-Br complex (NHC = N-heterocyclic carbene) as the precursor for the synthesis of thiolate-protected Au NCs (see Supporting Information for details). Au<sub>42</sub>(PET)<sub>32</sub> was obtained by chromatography separation (Figure S1). Electrospray ionization (ESI) mass spectrometry analysis on the purified product identified peaks of [Au<sub>42</sub>(PET)<sub>32</sub>]<sup>2+</sup>,  $[Au_{42}(PET)_{32}+2Cs]^{2+}$ , and  $[Au_{42}(PET)_{32}]^+$  (Figure 1A), and their experimental isotopic patterns match well with the calculated ones; thus, the obtained NC is Au<sub>42</sub>(PET)<sub>32</sub>. Its UV-vis absorption spectrum (Figure 1B, green profile) shows two major peaks at 375 and 806 nm, being identical with the structurally characterized Au<sub>42</sub>(BM)<sub>32</sub> (Figure S2A),<sup>32</sup> where BM = SCH<sub>2</sub>Ph. ESI together with absorption spectra confirms that Au<sub>42</sub>(PET)<sub>32</sub> should possess the same structure as that of Au<sub>42</sub>(BM)<sub>32</sub> nanorods except the carbon tail, i.e., a hexagonal close packed Au<sub>20</sub> kernel in Au<sub>42</sub>(PET)<sub>32</sub> (abbreviated Au<sub>42</sub> hereafter) and its protection by two pairs of interlocked Au<sub>4</sub>(SR)<sub>5</sub> staple motifs on the ends and six monomeric Au(SR)<sub>2</sub> motifs around its body (Figure 1C). Based on previous density functional theory (DFT) calculations,<sup>32</sup> the 806 nm peak arises from the HOMO-LUMO transition, and the 375 nm peak is from HOMO-1 to LUMO+2 and HOMO-2 to LUMO+1 (Figure 1D).

Interestingly, the PL spectrum of Au<sub>42</sub> in dichloromethane (DCM) shows dual emission in the NIR region (Figure 1B, gray profile), with peak wavelengths at 875 and 1040 nm, similar to  $Au_{42}(BM)_{32}$  (Figure S2B). The QY of  $Au_{42}$  in DCM under ambient conditions is 11.9% (measured by an integrating sphere), which surpasses the reported thiolate-protected NCs with NIR  $PL^{16-25,33,34}$  except  $Au_{38}S_2(SR)_{20}$ (NIR QY 15%, single emission).<sup>35</sup> The PL excitation spectra for the two emissions (I and II) are similar and also track the absorption profile (Figure S3), suggesting that both emissions are associated with the HOMO-LUMO transition (Au20kernel-based). Furthermore, PL I has a short lifetime (0.72 ns,

Received: August 26, 2022

Published: October 14, 2022





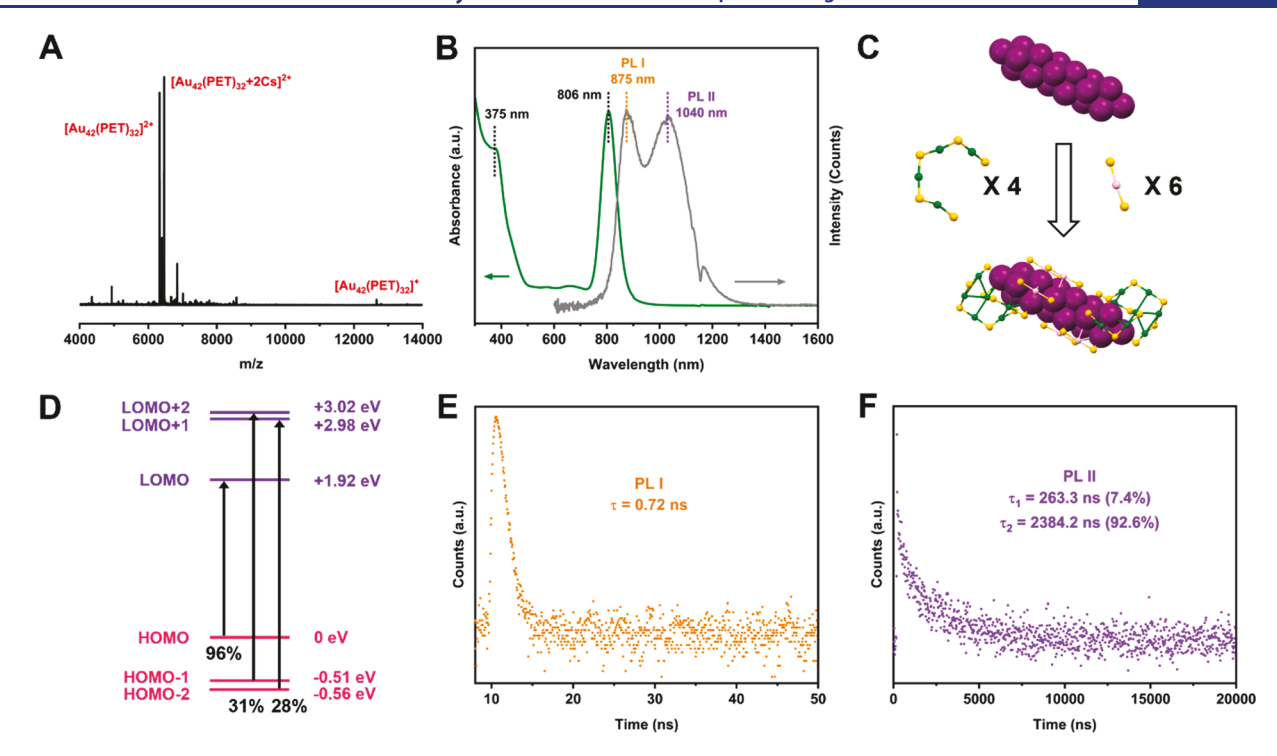


Figure 1. (A) ESI mass spectrum of  $Au_{42}$  (PET)<sub>32</sub>. (B) UV-vis absorption (green) and PL (gray) spectra of  $Au_{42}$  in DCM. (C) Structure of  $Au_{42}$  rod. Purple = core-Au, green = surface-Au, yellow = S, carbon tails omitted. (D) KS orbital diagram of  $Au_{42}$ . (E) Decay profile of PL I. (F) Decay profile of PL II. For PL measurements: excitation at 380 nm, slit width 4 nm, and emission slit 3.5 nm.

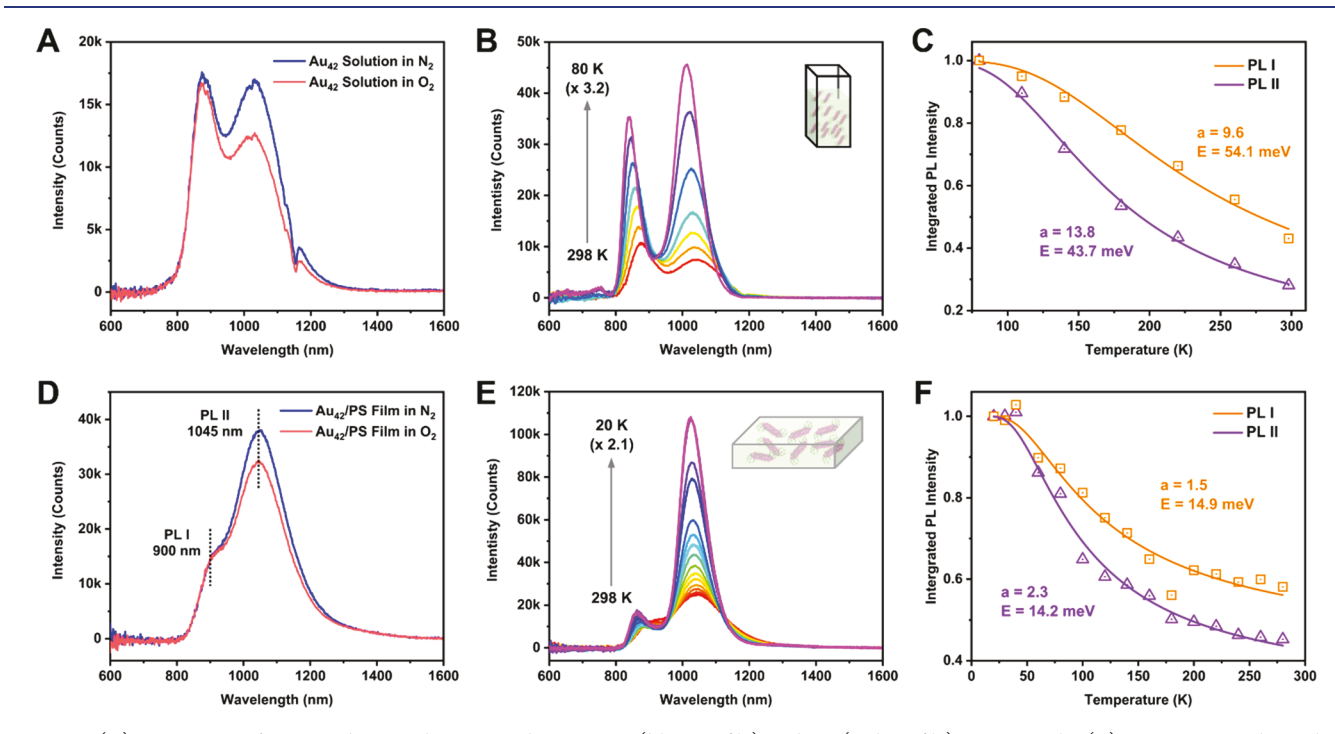


Figure 2. (A) PL spectra of  $Au_{42}$  in deaerated DCM under pure  $N_2$  (blue profile) and  $O_2$  (red profile), respectively. (B) Temperature-dependent PL spectra of  $Au_{42}$  in 2-methyletetrahydrofuran. (C) Normalized integrated PL I and II peak intensities and fitting using eq 1 (data from B). (D) PL spectra of  $Au_{42}$ /PS film under pure  $N_2$  (blue) and  $O_2$  (red), respectively. (E) Temperature-dependent PL spectra of  $Au_{42}$ /PS film. (F) Normalized integrated PL I and II peak intensities and fitting using eq 1 (data from E).

Figure 1E), which can be assigned as fluorescence, while PL II gives rise to a long lifetime up to 2.4  $\mu$ s, which should be a triplet emission (Figure 1F).

The dual emission of  $Au_{42}$  was further tested under pure  $N_2$  and  $O_2$ , respectively (Figure 2A). The overall integrated intensity of PL I and II was suppressed to 83% under pure  $O_2$ 

(Table S1). To quantitatively understand the evolution of the two bands, the PL spectra were deconvoluted into two Voigt profiles to extract the contribution from each peak (Figure S4A,B). As given in Table S1, the intensity of PL I almost remained the same under different gases, while PL II was quenched to 78% under pure  $O_2$ . The lifetime of PL II

drastically decreased from 2.4 µs to 1.5 µs, but PL I only slightly decreased from 0.72 ns to 0.64 ns (Figure S5). These results further confirm that PL I is fluorescence and PL II is phosphorescence. Considering the 0.12 eV Stokes shift (i.e., between the HOMO-LUMO peak and PL I) and the 0.2 eV difference between PL I and II, we deduce that the PL behavior of Au<sub>42</sub> follows Kasha's rule; that is, PL I is from the first excited singlet state (S<sub>1</sub>) and PL II from the first excited triplet state  $(T_1)$ .

To understand the nonradiative relaxation process in Au<sub>42</sub>, temperature-dependent steady-state PL measurements for Au<sub>42</sub> in 2-methyltetrahydrofuran were carried out (from room temperature down to 80 K, Figure 2B). To eliminate the effect of O2, the sample chamber of the cryostat was filled with helium gas during the experiment. Figure 2B shows that both PL peaks become sharper with a slight blue-shift as the temperature decreases from 298 K to 80 K, indicating a strong electron–phonon interaction in Au<sub>42</sub>. The integrated intensity of PL I and II was found to increase by 3.2 times from 298 to 80 K, which means that the QY reaches 38.1% at 80 K. We also performed peak deconvolution for all the temperature-dependent spectra and calculated the PL intensity relative ratios of PL I and II (Figure S6A). The PL II is found to account for 60% of the total PL intensity at room temperature, and its percentage rises to 70% at 80 K, which means that PL II is more favored at low temperatures than PL I, supporting the phosphorescence nature of PL II. Furthermore, the quantitative temperature-dependent intensity evolutions for both emission peaks are plotted in Figure 2C, where the PL intensity at the lowest temperature is set as unity. To analyze the temperature-dependent data for extracting information on the thermally activated nonradiative relaxation pathway, we adopt an Arrhenius expression (eq 1):<sup>37</sup>

$$I(T) = \frac{I_0}{1 + ae^{-E/k_B T}} \tag{1}$$

where  $I_0$  is the initial intensity, a is the ratio of nonradiative and radiative probabilities, and E is the activation energy for the nonradiative relaxation channel. Here, only one dominant phonon-assisted nonradiative channel is considered in our modeling. The resulted fit lines and parameters are given in Figure 2C, where the activation energies of phonon modes that are coupled with PL I and II are determined to be 54.1 and 43.7 meV, respectively. Based on previous theoretical and experimental work, 38-41 the two phonon modes (300-400 cm<sup>-1</sup>) can be assigned to the Au-S vibration of the two  $Au_4(SR)_5$  staple motifs on both ends of  $Au_{42}$ .

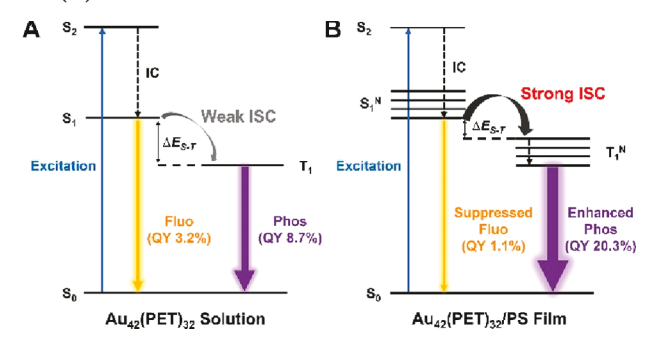
Given the facts that the dominant nonradiative relaxation channel in Au<sub>42</sub> solution is from the motif phonon mode and its NIR PLQY reaches 38.1% at 80 K, we rationalize that if the motif vibration can be suppressed at room temperature, the PL performance of Au<sub>42</sub> should be dramatically improved. To test our hypothesis, Au<sub>42</sub> NCs are embedded in a PS thin film via a drop-cast method. The emission spectrum of Au<sub>42</sub>/PS film at room temperature is shown in Figure 2D (blue curve), and excitation spectra are shown in Figure S7; indeed, the integrated intensity of PL I and II increases by 1.8 times compared to Au<sub>42</sub> in DCM, hence, an overall 21.4% QY for Au<sub>42</sub>/PS film. Interestingly, peak deconvolution results (Figure S4C, Table S1) find that the behavior of the two PL bands of films diverges: the QY of PL I decreases from 3.2% to 1.1% in the solid state, while the QY of PL II increases from 8.7% to 20.3%. The lifetimes of both PL I and II are slightly shorter in

the solid state (Figure S8). Furthermore, the emission of the Au<sub>42</sub>/PS film under O<sub>2</sub> (red line, Figure 2D) is quenched to 87% compared to the N<sub>2</sub> atmosphere. Further quantitative analysis (Figure S4D, Table S1) finds that only the intensity of PL II was significantly affected by the existence of O<sub>2</sub>, which is consistent with the solution results discussed above. The lifetimes of both PL bands become shorter under O<sub>2</sub> but within their respective nanosecond and microsecond scale, indicating the emission origins are unchanged.

To understand the divergent behavior of the two PL bands from solution to film state, we conducted cryogenic photoluminescence measurements for Au<sub>42</sub>/PS films (Figure 2E). The overall PL intensity of Au<sub>42</sub>/PS film increases by 2.1 times when the temperature decreases from room temperature to 20 K. In line with the solution results, PL II is more favored at low temperatures than PL I (Figure S6B), and both PL bands show a small blue-shift at low temperatures. After applying eq 1 to the data collected from the solid state (Figure 2F), we notice that both PL I and II are coupled with a phonon mode of ~14 meV (as opposed to ~50 meV in solution). Low-frequency phonon modes (<150 cm<sup>-1</sup>) are typically ascribed to the Au-Au vibration in the kernel of Au NCs. 40,42 Here, the 14 meV (112 cm<sup>-1</sup>) mode most likely originates from the breathing or extensional mode of the rod-like Au<sub>20</sub> kernel in Au<sub>42</sub>, but further theoretical simulations are required for confirmation. The *a* value (i.e., the ratio of nonradiative and radiative decays) also falls drastically from  $\sim 10$  (in solutions) to  $\sim 2$  (in films), indicating a significant suppression of the staple motif vibration-induced nonradiative decay. 33,40 Since the phononassisted nonradiative relaxation is suppressed for both PL I and II, one would expect to see that both PL I and II should have an equal enhancement of QY in the solid state, but this is not the case; rather, a divergent behavior was observed for PL I and II. Therefore, the expected enhancement of PL I must have been counteracted by another mechanism, which results in a net quenching of the fluorescence band from S1 in the

The counteracting mechanism should be S<sub>1</sub> to T<sub>1</sub> intersystem crossing (ISC), Scheme 1A. We rationalize that

Scheme 1. Emission Mechanism of Au<sub>42</sub>, (A) in Solutions and (B) in Films



the suppression of fluorescence and enhancement of phosphorescence from solution to film state should originate from dipole–dipole interactions. 43 According to Kasha's exciton model, dipolar interactions will cause a split in the excited state of the Au<sub>42</sub> dimer and narrow the gap between S<sub>1</sub> and T<sub>1</sub> states. 44 Such a model can be extended to assemblies where the split excited states become denser and yield a bandlike electronic structure (Scheme 1B), 45 evidenced by the 806

nm peak broadening in the film's UV—vis absorption spectrum (Figure S9). According to Fermi's golden rule, the intersystem crossing rate can be described by eq 2, 46

$$k_{\rm ISC} \propto \frac{|\langle \Psi_{\rm S}|H_{\rm S-O}|\Psi_{\rm T}\rangle|}{\Delta E_{\rm S-T}}$$
 (2)

where  $\Delta E_{\rm S-T}$  is the energy gap between singlet and triplet states,  $H_{\rm S-O}$  is the Hamiltonian describing the spin-orbit coupling, and  $\Psi_{\rm S}$  and  $\Psi_{\rm T}$  are wave functions for singlet and triplet states, respectively. Without any change in the structure of  ${\rm Au}_{42}$  between the solution and solid state, the difference in the perturbation term caused by spin-orbit coupling should be negligible. Therefore, when  $\Delta E_{\rm S-T}$  becomes smaller in the solid state, ISC is enhanced, hence, the phosphorescence (Scheme 1B). Considering the dipolar interaction is distance-dependent, we tested the PL of films with different  ${\rm Au}_{42}$  loadings to adjust the average distances among NCs and indeed observed a systematic trend of decreasing QY of PL I and increasing QY of PL II (Figure 3) as the  ${\rm Au}_{42}$  mass fraction increases, which provides substantial evidence for the proposed mechanism.

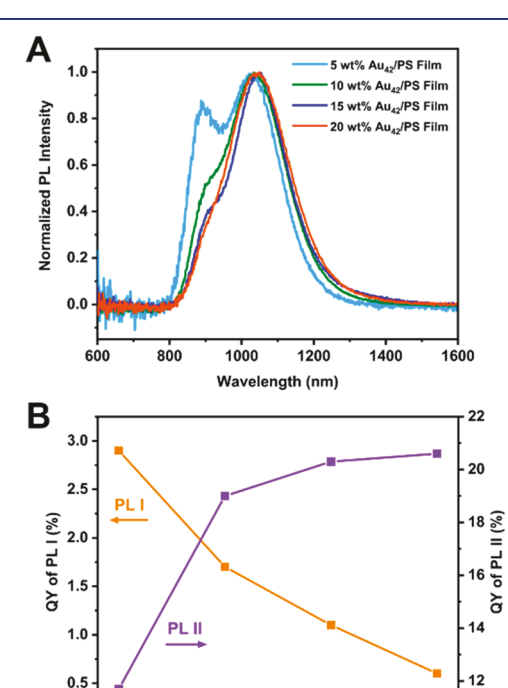


Figure 3. Photoluminescence properties of  $Au_{42}/PS$  films with different  $Au_{42}$  mass fractions. (A) Normalized PL spectra; (B) QYs of PL I and PL II versus mass fractions. All measurements were under  $N_2$ .

Mass fraction (wt%)

15

20

10

In summary, bright dual emission (PLQY = 11.9%) in the NIR region is attained in the  $\mathrm{Au}_{42}(\mathrm{PET})_{32}$ , which comprises fluorescence (QY = 3.2%) and phosphorescence (QY = 8.7%). After embedding  $\mathrm{Au}_{42}$  in films, the QY of phosphorescence significantly increases to 20.3% while the fluorescence is suppressed to 1.1% due to enhanced intersystem crossing. The efficient dual NIR emission makes  $\mathrm{Au}_{42}$  a promising candidate for future applications.

#### ASSOCIATED CONTENT

# **Solution** Supporting Information

The Supporting Information is available free of charge at https://pubs.acs.org/doi/10.1021/jacs.2c09107.

Additional synthesis and data analysis details (PDF)

## AUTHOR INFORMATION

## **Corresponding Author**

Rongchao Jin — Department of Chemistry, Carnegie Mellon University, Pittsburgh, Pennsylvania 15213, United States; orcid.org/0000-0002-2525-8345; Email: rongchao@andrew.cmu.edu

#### **Authors**

Lianshun Luo — Department of Chemistry, Carnegie Mellon University, Pittsburgh, Pennsylvania 15213, United States; orcid.org/0000-0001-6158-6672

Zhongyu Liu — Department of Chemistry, Carnegie Mellon University, Pittsburgh, Pennsylvania 15213, United States; orcid.org/0000-0002-2777-8360

Xiangsha Du — Department of Chemistry, Carnegie Mellon University, Pittsburgh, Pennsylvania 15213, United States; orcid.org/0000-0002-6508-866X

Complete contact information is available at: https://pubs.acs.org/10.1021/jacs.2c09107

## **Author Contributions**

<sup>#</sup>L.L. and Z.L. contributed equally to this work.

#### Notes

The authors declare no competing financial interest.

## ACKNOWLEDGMENTS

R.J. thanks the funding support from NSF (DMR 1808675).

# REFERENCES

- (1) Kang, X.; Zhu, M. Tailoring the photoluminescence of atomically precise nanoclusters. *Chem. Soc. Rev.* **2019**, *48*, 2422–2457.
- (2) Marin, R.; Jaque, D. Doping Lanthanide Ions in Colloidal Semiconductor Nanocrystals for Brighter Photoluminescence. *Chem. Rev.* **2021**, *121*, 1425–1462.
- (3) Wan, X.-K.; Xu, W. W.; Yuan, S.-F.; Gao, Y.; Zeng, X.-C.; Wang, Q.-M. A Near-Infrared-Emissive Alkynyl-Protected Au<sub>24</sub> Nanocluster. *Angew. Chem. Int. Ed.* **2015**, *54*, 9683–9686.
- (4) Chen, T.; Lin, H.; Cao, Y.; Yao, Q.; Xie, J. Interactions of Metal Nanoclusters with Light: Fundamentals and Applications. *Adv. Mater.* **2022**, *34*, 2103918.
- (5) Sugiuchi, M.; Maeba, J.; Okubo, N.; Iwamura, M.; Nozaki, K.; Konishi, K. Aggregation-Induced Fluorescence-to-Phosphorescence Switching of Molecular Gold Clusters. *J. Am. Chem. Soc.* **2017**, *139*, 17731–17734.
- (6) Maity, S.; Bain, D.; Patra, A. An Overview on the Current Understanding of the Photophysical Properties of Metal Nanoclusters and Their Potential Applications. *Nanoscale* **2019**, *11*, 22685–22723.
- (7) Kumar, A. S. K.; Tseng, W. L. Perspective on Recent Developments of Near Infrared-Emitting Gold Nanoclusters: Applications in Sensing and Bio-Imaging. *Anal. Methods* **2020**, *12*, 1809–1826.
- (8) Pyo, K.; Ly, N. H.; Han, S. M.; Hatshan, M.; Abuhagr, A.; Wiederrecht, G.; Joo, S.-W.; Ramakrishna, G.; Lee, D. Unique Energy Transfer in Fluorescein-Conjugated Au<sub>22</sub> Nanoclusters Leading to 160-Fold pH-Contrasting Photoluminescence. *J. Phys. Chem. Lett.* **2018**, *9*, 5303–5310.
- (9) Khatun, E.; Bodiuzzaman, M.; Sugi, K. S.; Chakraborty, P.; Paramasivam, G.; Dar, W. A.; Ahuja, T.; Antharjanam, S.; Pradeep, T.

- Confining an  $Ag_{10}$  Core in an  $Ag_{12}$  Shell: A Four-Electron Superatom with Enhanced Photoluminescence upon Crystallization. *ACS Nano* **2019**, *13*, 5753–5759.
- (10) Zhang, M.-M.; Dong, X.-Y.; Wang, Z.-Y.; Luo, X.-M.; Huang, J.-H.; Zang, S.-Q.; Mak, T. C. W. Alkynyl-Stabilized Superatomic Silver Clusters Showing Circularly Polarized Luminescence. *J. Am. Chem. Soc.* 2021, 143, 6048–6053.
- (11) Su, Y. M.; Ji, B. Q.; Wang, Z.; Zhang, S. S.; Feng, L.; Gao, Z. Y.; Li, Y. W.; Tung, C. H.; Sun, D.; Zheng, L. S. Anionic Passivation Layer-assisted trapping of an Icosahedral Ag<sub>13</sub> Kernel in a Truncated Tetrahedral Ag<sub>89</sub> Nanocluster. *Sci. China Chem.* **2021**, *64*, 1482–1486
- (12) Andolina, C. M.; Crawford, S. E.; Smith, A. M.; Johnston, K. A.; Straney, P. J.; Marbella, L. E.; Tolman, N. L.; Hochuli, T. J.; Millstone, J. E. Near-Infrared Photoluminescence from Small Copper, Silver, and Gold Nanoparticles. *ChemNanoMat* **2018**, *4*, 265–268.
- (13) Pramanik, G.; Humpolickova, J.; Valenta, J.; Kundu, P.; Bals, S.; Bour, P.; Dracinsky, M.; Cigler, P. Gold Nanoclusters with Bright Near-Infrared Photoluminescence. *Nanoscale* **2018**, *10*, 3792–3798.
- (14) Behera, S. K.; Park, S. Y.; Gierschner, J. Dual Emission: Classes, Mechanisms, and Conditions. *Angew. Chem., Int. Ed.* **2021**, *60*, 22624–22638.
- (15) Huang, X.; Song, J.; Yung, B. C.; Huang, X.; Xiong, Y.; Chen, X. Ratiometric Optical Nanoprobes Enable Accurate Molecular Detection and Imaging. *Chem. Soc. Rev.* **2018**, *47*, 2873–2920.
- (16) Wu, Z.; Yao, Q.; Zang, S.-q.; Xie, J. Aggregation-Induced Emission in Luminescent Metal Nanoclusters. *Natl. Sci. Rev.* **2021**, 8, nwaa208.
- (17) Weerawardene, K. L. D. M.; Aikens, C. M. Theoretical Insights into the Origin of Photoluminescence of  $\mathrm{Au}_{25}(\mathrm{SR})_{18}^-$  Nanoparticles. J. Am. Chem. Soc. **2016**, 138, 11202–11210.
- (18) Li, Q.; Zhou, D.; Chai, J.; So, W. Y.; Cai, T.; Li, M.; Peteanu, L. A.; Chen, O.; Cotlet, M.; Wendy Gu, X.; Zhu, H.; Jin, R. Structural Distortion and Electron Redistribution in Dual-Emitting Gold Nanoclusters. *Nat. Commun.* **2020**, *11*, 2897.
- (19) Li, Q.; Zeman, C. J., IV; Ma, Z.; Schatz, G. C.; Gu, X. W. Bright NIR-II Photoluminescence in Rod-Shaped Icosahedral Gold Nanoclusters. *Small* **2021**, *17*, 2007992.
- (20) Mitsui, M.; Wada, Y.; Kishii, R.; Arima, D.; Niihori, Y. Evidence for Triplet-State-Dominated Luminescence in Biicosahedral Superatomic Molecular Au<sub>25</sub> Clusters. *Nanoscale* **2022**, *14*, 7974–7979.
- (21) Wu, Z.; Yao, Q.; Chai, O. J. H.; Ding, N.; Xu, W.; Zang, S.; Xie, J. Unraveling the Impact of Gold(I)-Thiolate Motifs on the Aggregation-Induced Emission of Gold Nanoclusters. *Angew. Chem., Int. Ed.* **2020**, *59*, 9934–9939.
- (22) Herbert, P. J.; Ackerson, C. J.; Knappenberger, K. L. Size-Scalable Near-Infrared Photoluminescence in Gold Monolayer Protected Clusters. *J. Phys. Chem. Lett.* **2021**, *12*, 7531–7536.
- (23) Zhou, M.; Song, Y. B. Origins of Visible and Near-Infrared Emissions in [Au<sub>25</sub>(SR)<sub>18</sub>]<sup>-</sup> Nanoclusters. *J. Phys. Chem. Lett.* **2021**, 12, 1514–1519.
- (24) Gan, Z.; Lin, Y.; Luo, L.; Han, G.; Liu, W.; Liu, Z.; Yao, C.; Weng, L.; Liao, L.; Chen, J.; Liu, X.; Luo, Y.; Wang, C.; Wei, S.; Wu, Z. Fluorescent Gold Nanoclusters with Interlocked Staples and a Fully Thiolate-Bound Kernel. *Angew. Chem., Int. Ed.* **2016**, *55*, 11567–11571.
- (25) Bertorelle, F.; Wegner, K. D.; Bakulić, M. P.; Fakhouri, H.; Comby-Zerbino, C.; Sagar, A.; Bernadó, P.; Resch-Genger, U.; Bonačić-Koutecký, V.; Le Guével, X.; Antoine, R. Tailoring the NIR-II Photoluminescence of Single Thiolated Au<sub>25</sub> Nanoclusters by Selective Binding to Proteins. *Chem.-A Eur. J.* **2022**, 28, No. e202200570.
- (26) Aikens, C. M. Electronic and Geometric Structure, Optical Properties, and Excited State Behavior in Atomically Precise Thiolate-Stabilized Noble Metal Nanoclusters. *Acc. Chem. Res.* **2018**, *51*, 3065–3073.
- (27) Jin, R.; Li, G.; Sharma, S.; Li, Y.; Du, X. Toward Active-Site Tailoring in Heterogeneous Catalysis by Atomically Precise Metal

- Nanoclusters with Crystallographic Structures. Chem. Rev. 2021, 121, 567–648.
- (28) Zhou, C.; Hao, G.; Thomas, P.; Liu, J.; Yu, M.; Sun, S.; Öz, O. K.; Sun, X.; Zheng, J. Near-Infrared Emitting Radioactive Gold Nanoparticles with Molecular Pharmacokinetics. *Angew. Chem., Int. Ed.* **2012**, *51*, 10118–10122.
- (29) Ma, H.; Wang, J.; Zhang, X.-D. Near-Infrared II Emissive Metal Clusters: from Atom Physics to Biomedicine. *Coord. Chem. Rev.* **2021**, 448, 214184.
- (30) Rad, A. T.; Bao, Y.; Jang, H.-S.; Xia, Y.; Sharma, H.; Dormidontova, E. E.; Zhao, J.; Arora, J.; John, V. T.; Tang, B. Z.; Dainese, T.; Hariri, A.; Jokerst, J. V.; Maran, F.; Nieh, M.-P. Aggregation-Enhanced Photoluminescence and Photoacoustics of Atomically Precise Gold Nanoclusters in Lipid Nanodiscs (NANO<sup>2</sup>). *Adv. Funct. Mater.* **2021**, *31*, 2009750.
- (31) Peng, C. Q.; Yu, M. X.; Zheng, J. In Situ Ligand-Directed Growth of Gold Nanoparticles in Biological Tissues. *Nano Lett.* **2020**, 20, 1378–1382.
- (32) Li, Y.; Song, Y.; Zhang, X.; Liu, T.; Xu, T.; Wang, H.; Jiang, D.e.; Jin, R. Atomically Precise Au<sub>42</sub> Nanorods with Longitudinal Excitons for an Intense Photothermal Effect. *J. Am. Chem. Soc.* **2022**, 144, 12381–12389.
- (33) Li, Q.; Zhou, M.; So, W. Y.; Huang, J.; Li, M.; Kauffman, D. R.; Cotlet, M.; Higaki, T.; Peteanu, L. A.; Shao, Z. A Mono-Cuboctahedral Series of Gold Nanoclusters: Photoluminescence Origin, Large Enhancement, Wide Tunability, and Structure—Property Correlation. J. Am. Chem. Soc. 2019, 141, 5314—5325.
- (34) Wu, Z.; Jin, R. On the Ligand's Role in the Fluorescence of Gold Nanoclusters. *Nano Lett.* **2010**, *10*, 2568–2573.
- (35) Li, Q.; Zeman, C. J., IV; Schatz, G. C.; Gu, X. W. Source of Bright Near-Infrared Luminescence in Gold Nanoclusters. *ACS Nano* **2021**, *15*, 16095–16105.
- (36) Devadas, M. S.; Bairu, S.; Qian, H.; Sinn, E.; Jin, R.; Ramakrishna, G. Temperature-Dependent Optical Absorption Properties of Monolayer-Protected Au<sub>25</sub> and Au<sub>38</sub> Clusters. *J. Phys. Chem. Lett.* **2011**, *2*, 2752–2758.
- (37) Steele, J. A.; Puech, P.; Monserrat, B.; Wu, B.; Yang, R. X.; Kirchartz, T.; Yuan, H.; Fleury, G.; Giovanni, D.; Fron, E. Role of Electron—Phonon Coupling in the Thermal Evolution of Bulk Rashba-Like Spin-Split Lead Halide Perovskites Exhibiting Dual-Dand Photoluminescence. ACS Energy Lett. 2019, 4, 2205—2212.
- (38) Tlahuice-Flores, A.; Whetten, R. L.; Jose-Yacaman, M. Vibrational Normal Modes of Small Thiolate-Protected Gold Clusters. J. Phys. Chem. C 2013, 117, 12191–12198.
- (39) Bürgi, T. Properties of the Gold–Sulphur Interface: from Self-Assembled Monolayers to Clusters. *Nanoscale* **2015**, *7*, 15553–15567.
- (40) Liu, Z.; Li, Y.; Shin, W.; Jin, R. Observation of Core Phonon in Electron–Phonon Coupling in Au<sub>25</sub> Nanoclusters. *J. Phys. Chem. Lett.* **2021**, *12*, 1690–1695.
- (41) Nieto-Ortega, B.; Bürgi, T. Vibrational Properties of Thiolate-Protected Gold Nanoclusters. *Acc. Chem. Res.* **2018**, *51*, 2811–2819.
- (42) Kato, M.; Shichibu, Y.; Ogura, K.; Iwasaki, M.; Sugiuchi, M.; Konishi, K.; Yagi, I. Terahertz Raman Spectroscopy of Ligand-Protected Au<sub>8</sub> Clusters. *J. Phys. Chem. Lett.* **2020**, *11*, 7996–8001.
- (43) Li, Y.; Cowan, M. J.; Zhou, M.; Taylor, M. G.; Wang, H.; Song, Y.; Mpourmpakis, G.; Jin, R. Heterometal-Doped  $M_{23}$  (M = Au/Ag/Cd) Nanoclusters with Large Dipole Moments. *ACS Nano* **2020**, *14*, 6599–6606.
- (44) Kasha, M.; Rawls, H. R.; El-Bayoumi, M. A. The Exciton Model in Molecular Spectroscopy. *Pure Appl. Chem.* **1965**, *11*, 371–392.
- (45) Yang, L.; Wang, X.; Zhang, G.; Chen, X.; Zhang, G.; Jiang, J. Aggregation-Induced Intersystem Crossing: a Novel Strategy for Efficient Molecular Phosphorescence. *Nanoscale* **2016**, *8*, 17422–17426.
- (46) Hirai, H.; Takano, S.; Nakashima, T.; Iwasa, T.; Taketsugu, T.; Tsukuda, T.Doping-Mediated Energy-Level Engineering of M@Au<sub>12</sub> Superatoms (M= Pd, Pt, Rh, Ir) for Efficient Photoluminescence and PhotocatalysisAngew. Chem., Int. Ed.2022, e202207290, DOI: 10.1002/anie.202207290.